Electronic Research Archive

ERA, 33(4): 2412–2432.
DOI: 10.3934/era.2025107
Received: 12 January 2025
Revised: 24 March 2025
Accepted: 08 April 2025
Published: 22 April 2025

https://www.aimspress.com/journal/ERA

Research article

Complex visual cognitive function based on a large-scale neurovascular and metabolic coupling mechanisms model in whole brain

Tongna Wang, Bao Li, Youjun Liu, Ruoyao Xu, Yuejuan Xu, Yang Yang and Liyuan Zhang*

Department of Biomedical Engineering, Beijing University of Technology, 100 Pingleyuan, Chaoyang District, Beijing 100124, China

* **Correspondence:** Email: LiyuanZhang@bjut.edu.cn.

Supplementary

1. Preprocessing

1.1. EEG data preprocessing

The EEG data were preprocessed using EEGLAB2023.0 and the process included the removal of unwanted leads, filtering with low-pass and high-pass filters from 0.1 hz to 30 hz, pulse artifact was then removed using ICA, empirical removal of ophthalmic and electromyographic noise. At the same time, in order to better observe the changes in neural activity induced by the task state, we extracted the average event-related potentials (ERP) of EEG for subsequent computations.

1.2. MRI data preprocessing

The MRI data were preprocessed using SPM12 (http://www.fil.ion.ucl.ac.uk/spm). The first volumes were corrected for the acquisition time delay between slices. In MRI, we estimated subject head motion immediately after the MRI scans to ensure that all participants' data were within the defined motion thresholds (i.e., translational or rotational motion parameters less than 2 mm or 2°).

1.3. fMRI data preprocessing

The fMRI data were preprocessed using SPM12 (http://www.fil.ion.ucl.ac.uk/spm). The first 10 volumes for each participant were discarded to allow the signal to reach equilibrium and the participants to adapt to the scanning noise. Similar to MRI pre-processing, the remaining volume was time-layer corrected according to the acquisition time delay between slices, and after that, we performed head movement correction, i.e., we immediately assessed the head movements of the subjects to ensure that the BOLD data of all the participants were within the defined movement thresholds. In the normalization step, individual structural images were linearly co-registered with the mean functional image; then the transformed structural images were segmented into gray matter, white matter, and cerebrospinal fluid. The gray matter maps were nonlinearly co-registered with the tissue probability maps in the Montreal Neurological Institute (MNI) space. Finally, each filtered functional volume was spatially normalized to MNI space using the parameters estimated during nonlinear co-registration. The functional images were then resampled into a voxel size of $3 \times 3 \times 3$ mm^3.

2. Dynamic modelling

At present, the research on complex brain networks is usually based on the macroscopic and large-scale level. The choice of a brain parcellation scheme is used to define brain regions-of-interest (ROIs), and most of them use some prior brain region maps to divide the brain, such as an automated anatomical labeling (AAL) atlas [1], Hagmann atlas [2], Desikan-Killiany (DK) atlas [3], Brodmann atlas et al. [4]. In this study, DK atlas was used to divide the image data into distinct regions.

Functional connectivity describes the degree to which any two nodes of the brain are functionally related under a given cognitive task. The whole-brain LFP is the activation level of neuronal clusters in brain regions obtained from actual EEG reconstruction. Since LFP is based on the brain region level, the LFP time series of each ROI was first extracted separately, and then the Pearson correlation coefficients of the time series of any two ROIs were computed to obtain the $N \times N$ brain network functional connectivity matrix (N is the number of ROIs, $N \leq 68$).

Firstly, based on the preprocessed and personalized MRI data, the averaged ERP data were converted to dipoles in cortical space using the brainstorm3 toolbox(https://neuroimage.usc.edu/brainstorm/Introduction), and the method used for this process was the sLORETA inverse transformation. Secondly, the central dipoles of each brain region were obtained based on the DK partition in order to construct a simplified distributed dipole model. Lastly, the activity of the cortical central dipole was considered as the neural dynamic energy used to drive the model. Inverse transformation was processed with software tools in brainstorm.

2.1. Reconstruction of the local field potential

Since pyramidal neurons are perpendicular to the cortical surface, with dendrites facing the cortical surface and axons pointing to the grey matter-white matter border, the central dipole orientation is also set perpendicular to the cortical surface. The dipole theory is used to reconstruct the local field potentials (LFPs) and the theory of Demont-Guignard (2009) is considered in this study [5]. The assumptions include, on the one hand, that each neuronal mass model is considered as a dipole, located in a brain tissue with uniform conductivity ($\sigma = 1$), on the other hand, according to the

superposition theory, the total LFP of a given brain region is the instantaneous summation of itself and the contribution of the remaining brain regions. The specific LFP formula is as follows:

$$V = \sum_{i=1}^{N} \frac{\vec{d_i} \cdot \vec{u_i}}{4\pi\sigma {r_i}^2} \tag{1}$$

where σ is the conductivity, r_i is the distance from cell i to the measurement point (i.e., the recording electrode), $\vec{u}_i$ is a unit vector on a straight line from neuron i to the recording point d_i, $\vec{d}_i$ is the dipole moment, and N is the total number of brain regions (N ≤ 68).

2.2. Formulation and establishment of reverse neural mass model

The dynamic modelling was derived by neural mass model (NMM) [6] which is the lumped-state variable is used to represent the average behavior within each brain region to the following set of nonlinear differential equations. The NMM including two sub-populations corresponding to pyramidal cells and interneurons, respectively. The linear transformation function labeled $H_{exc}(t)$ and $H_{inh}(t)$, convert presynaptic potentials (mean pulse density of action potentials) to postsynaptic potentials (excitatory postsynaptic potential (EPSP) and inhibitory postsynaptic potential (IPSP)).

$$\begin{aligned} &\dot{z}(t) = z_1(t) \\ &\dot{z}_1(t) = Ggx(t) - 2gz_1(t) - g^2 z(t) \\ &H_{exc}(t) = Aae^{-at}, \ H_{inh}(t) = Bbe^{-at} \\ &S(v) = 2e_0/(1 + e^{r(v_0 - v)}) \end{aligned} \tag{2}$$

where *A* is the excitatory synaptic gain and *B* is the inhibitory synaptic gain. Parameters $H_{exc}(t)$ and $H_{inh}(t)$ are the excitatory and inhibitory mean synaptic gains which are used to regulate the postsynaptic potential (PSP), respectively. These four parameters of A, B, a, and b can regulate the sensitivity of excitatory and inhibitory synapses and determine the excitatory and inhibitory properties of the model. $2e_0$ is the maximum firing rate of the neural population, v_0 is PSP relatives to the e_0, r the steepness of the sigmoidal transformation, and v is the presynaptic mean membrane potential. G and g denote the parameters $h_e(t)$ in the excitability condition or the parameters $h_i(t)$ in the suppression condition. In the excitatory case, G = A, g = a, and in the inhibitory case, G = B, g = b. $x(t)$ and $z(t)$ are the input and output signals of the sub-populations, respectively.

The difference between the reverse neural mass model (RNMM) and NMM is that RNMM has no noise input $p(t)$, such as white noise. The input of RNMM is LFP obtained from section 2.4, which corresponds to position of the LFP output of the NMM. Using the following differential equations to describe the whole-brain reverse neural mass model (wRNMM):

$$\begin{aligned} \dot{y}_0^n(t) &= y_3^n(t) \\ \dot{y}_3^n(t) &= A * a * S_1\left[LFP_{input}\right] - 2 * a * y_3^n(t) - a^2 * y_0^n(t) \\ \dot{y}_1^n(t) &= y_4^n(t) \\ \dot{y}_4^n(t) &= A * a * \{C2 * S_1[C1 * y_0^n] + \sum_{i=1,\ldots,N, i\neq n} k_{in}\, y_6^i(t)\} - 2 * a * y_4^n(t) - a^2 * y_1^n(t) \\ \dot{y}_2^n(t) &= y_5^n(t) \end{aligned} \tag{3}$$

$$\dot{y}_5^n(t) = B * b * \{C4 * S_2[C3 * y_0^n]\} - 2 * b * y_5^n(t) - b^2 * y_2^n(t)$$
$$\dot{y}_6^n(t) = y_7^n(t)$$
$$\dot{y}_7^n(t) = A * \left(\frac{a}{3}\right) * S_1\left[LFP_{output}\right] - 2 * \left(\frac{a}{3}\right) * y_7^n(t) - \left(\frac{a}{3}\right)^2 * y_6^n(t)$$
$$LFP_{output} = y_1^n(t) - y_2^n(t)$$
$$C_1 = C \quad C_2 = 0.8 * C \quad C_3 = 0.25 * C \quad C_4 = 0.25 * C$$

where y_0, y_1 and y_2 are the outputs of the three PSP blocks, respectively. y_6 is the contribution of the current node to all other nodes. Connectivity constants k_{in}, attenuate the output of i column before it is fed to the n column. The above system of differential equations is solved using the ode45 method.

LFP_{input} was firstly normalized to ensure that its magnitude was similar to LFP_{output}. To ensure the accuracy of the PSP, the values of A, B, and C are adjusted to maximize the match between the LFP_{input} and LFP_{output}. The optimization method was simulated annealing method, and the error cost function was root mean square error (*RMSE*):

$$RMSE = \sqrt{\frac{\sum_1^n \left(LFP_{input} - LFP_{output}\right)^2}{n}} \tag{4}$$

where n is the number of samples in the LFP.

2.3. Description of metabolic hemodynamic modeling

The simulated neural activities $u_e(t)$ and $u_i(t)$ are fed to the Balloon-Windkessel hemodynamic model [7] to simulate the hemodynamic indexes for each ROI. Briefly, Changes in PSP, represented by $u_e(t)$ and $u_i(t)$ are linked to the corresponding changes in glucose consumption $g_e(t)$ and $g_i(t)$ by means of linear differential equations, respectively. Then, the total glucose consumption is calculated as a weighted average of the excitatory and inhibitory contributions. The glucose variables were then directly related to the metabolic rates of oxygen for excitatory $m_{\mathrm{e}}(t)$ and inhibitory $m_{\mathrm{i}}(t)$ activities, as well as to the total oxygen consumption $m(t)$. The interpretation and values of MHM parameters are displayed in Table 1. The equations relating these biological processes are as follows. The consumption of glucose for excitatory and inhibitory activities, respectively, and the total consumption is given by the following equation:

$$\begin{aligned}
&\dot{g}_e(t) = s_e(t)\\
&s_e(t) = \frac{a_e}{\tau_e}(u_e(t-\delta_e) - 1) - \frac{2}{\tau_e}s_e(t) - \frac{1}{\tau_e^2}(g_e(t) - 1)\\
&\dot{g}_i(t) = s_i(t)\\
&s_i(t) = \frac{a_i}{\tau_i}(u_i(t-\delta_i) - 1) - \frac{2}{\tau_i}s_i(t) - \frac{1}{\tau_i^2}(g_i(t) - 1)\\
&g(t) = \frac{2\gamma g_e(t) + (2-x_0)g_i(t)}{2\gamma + 2 - x_0}
\end{aligned} \tag{5}$$

The equations of total oxygen consumption m(t) are as follows:

$$m(t) = \frac{\gamma m_e(t) + m_i(t)}{\gamma + 1} = \frac{\gamma \frac{2-x(t)}{2-x_0}\, g_e(t) + g_i\ (t)}{\gamma + 1} \tag{6}$$

As in the study of Sotero and Trujillo-Barreto [7] there are specific details of the derivation of the equations describing this relationship. For describing CBF dynamics, the MHM uses the model introduced but with the additional assumption that CBF is not coupled to inhibitory activity. The MHM modifies the previous model [8], with the additional assumption that CBF is not coupled to inhibitory activity.

$$\begin{aligned} \dot{f}(t) &= s_f(t) \\ \dot{s}_f(t) &= \varepsilon\big(u_e\big(t-\delta_f\big)-1\big) - \tfrac{1}{\tau_s}s_f(t) - \tfrac{f(t)-1}{\tau_f} \end{aligned} \tag{7}$$

At the same time, the Balloon model [9] is employed for linking the output of the metabolic and vascular models to normalized cerebral blood volume (v) and deoxyhemoglobin content (q). Knowing q and v, the BOLD signal is calculated as in [9].

$$\begin{aligned} \dot{v}(t) &= \tfrac{1}{\tau_0}(f(t) - f_{out}(v,t)) \\ \dot{q}(t) &= \tfrac{1}{\tau_0}(m(t) - f_{out}(v,t)\tfrac{q(t)}{v(t)}) \\ f_{out}(v,t) &= v^{\frac{1}{\alpha}} + \tau\dot{v}(t) \end{aligned} \tag{8}$$

Given q and v, the BOLD signal is described as:

$$BOLD = V_0(a_1(1-q) - a_2(1-v)) \tag{9}$$

Table 1. Interpretation and values of the parameters used in the simulations.

Parameter	Interpretation	Value
a_e	Efficacy of glucose consumption response to excitation	1
a_i	Efficacy of glucose consumption response to inhibition	1
τ_e	Time-constant of the excitatory glucose consumption impulse response	1
τ_i	Time-constant of the inhibitory glucose consumption impulse response	0.8
c	Steepness of the sigmoid function x	2.5
d	Position of the threshold of the sigmoid function x	1.6
δ_e	Delay between excitatory neuronal activity and corresponding glucose consumption.	0.1 s
δ_i	Delay between inhibitory neuronal activity and corresponding glucose consumption	0.1 s
δ_f	Delay between excitatory neuronal activity and CBF response	0.2 s
γ	Baseline ratio of excitatory to inhibitory synaptic activity in the voxel	5
ε	Efficacy of blood flow response to excitation	0.6
τ_s	Constant for CBF signal decay	1.5
τ_f	Constant for CBF autoregulatory feedback	2.4
τ_0	Transit time through the balloon	1s
α	Coefficient of the steady state flow–volume relationship	0.4
a_1	Weight for deoxyhemoglobin change	3.4
a_2	Weight for blood volume change	1
V_0	Baseline blood volume	0.02

3. Brain network analysis

3.1. Average degree

The degree of a node represents the sum of the information transfer of that node, i.e., the number of edges that exist connected to other nodes through that node, and is also equal to the number of pro-anodes of that node. The greater the degree, the more important the node would be. The degree of a node is given by the following formula:

$$D_i = \sum_{j=1}^{N} w_{ij} \tag{10}$$

where w_{ij} is the element of the weighted undirected matrix and N is the scale of the matrix, i.e., N is the number of nodes. Where the average value of node degree indicates the sparsity of the network:

$$\overline{D} = \frac{1}{N}\sum_i D_i \tag{11}$$

A larger value of the average degree indicates a denser presence of edges between nodes in the network [10].

3.2. Clustering coefficient

The clustering coefficient reflects the degree of intensity between the nearby nodes of a given node, i.e., the likelihood of mutual neighbors between the nearby nodes of a node. The brain often works not as a single brain region works, but inter-brain regions are connected to each other and synergize to transmit information, and the clustering coefficient is the degree of synergy between brain regions. The larger the clustering coefficient of a node, the more important that node is in the network. The clustering coefficient of node i in the network is:

$$C_i = \frac{2t_i^w}{k_i(k_i-1)} \tag{12}$$

where weighted geometric mean of triangles around i, $t_i^{\mathrm{w}} = \frac{1}{2}\sum_{j,h\in N}\left(w_{ij}w_{ih}w_{jh}\right)^{1/3}$. $k_i(k_i-1)$ is the maximum number of possible polygons between these neighboring nodes. The average clustering coefficient of all nodes in the network is defined as the clustering coefficient of the network:

$$C = \frac{1}{N}\sum_i C_i \tag{13}$$

The clustering coefficient is a measure of functional segregation, which is the ability for specialized processing to occur within densely interconnected groups of brain regions [10].

3.3. Characteristic path length

Characteristic path length (CPL) plays an important role in the process of information transfer in brain networks. CPL is the average of the shortest path length between any two nodes in a network. The shortest path length can transfer information faster and reduce the consumption of the brain. The shorter the characteristic path length in the network, the more stable the network is and the higher the information transfer efficiency, on the contrary, the longer the characteristic path length, the more unstable the network is and the information transfer efficiency is relatively low. The characteristic path length of node i is:

$$l_{ij} = \sum_{i\in N} \frac{\sum_{j\in N, j\neq i} d_{ij}^{w}}{N-1}, d_{ij}^{w} = \sum_{a_{uv}\in gi\leftarrow j}^{w} f(w_{uv}) \tag{14}$$

where d_{ij}^{w} is the shortest weighted path length between i and j, where f is a map (e.g., an inverse) from weight to length. l_{ij} is the shortest path between node i and node j. The shortest path length of all nodes in the network is defined as the characteristic path length of the network:

$$L = \frac{1}{N}\sum_{i} l_i \tag{15}$$

The characteristic path length is a measure of functional integration, which is the ability to rapidly combine pieces of specialized information from distributed brain regions [10].

3.4. Betweenness centrality

In graph theory, betweenness centrality quantifies the importance of node within a graph by measuring its involvement in shortest paths. In a connected graph, there is at least one shortest path between any pair of nodes, where the shortest path either minimizes the number of edges traversed (for unweighted graphs) or the sum of edge weights (for weighted graphs). The betweenness centrality of a vertex is determined by the number of these shortest paths that pass through it.

The betweenness centrality of a node v is given by the expression:

$$g(v) = \sum_{s\neq v\neq t} \frac{\sigma_{st}(v)}{\sigma_{st}} \tag{16}$$

where σ_{st} is the total number of shortest paths from node s to node t. $\sigma_{st}(v)$ is the number of those paths that pass through v (s or t can be v) [11].

4. Optimization of resting-state LFP data

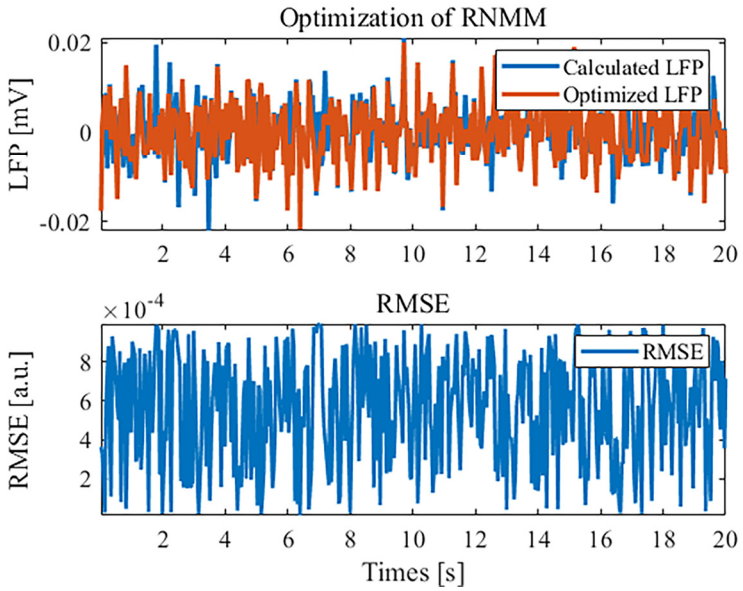

Figure 1. Optimization of resting-state LFP data.

5. Correlation analysis between individual variables and hemodynamic indices

Table 2. Correlation analysis between individual variables and hemodynamic indices.

Parameter	All patients (N = 16)	Spearman	Famous		Scrambled		Unfamiliar	
			FCS	CBF	FCS	CBF	FCS	CBF
Stimuli num	4–6	*r*-value	0.1208	– 0.2069	0.0428	– 0.2113	– 0.0562	– 0.1656
		P-value	0.2795	0.0622	0.7028	0.0567	0.6162	0.1370
Age	26.3415 ± 2.73622	*r*-value	**0.3016**	– 0.1886	– 0.0305	– 0.0342	0.0777	– 0.1077
		P-value	**0.0059**	0.0896	0. 7856	0.7601	0.4879	0.3383
Gender	Male = 9 Female = 7	*r*-value	– 0.0513	0.0704	0.0544	0.0839	0.0720	0.1211
		P-value	0.6475	0.5296	0.6276	0.4538	0.5206	0.2783

6. Hemodynamic metrics induced by neural activities of different durations

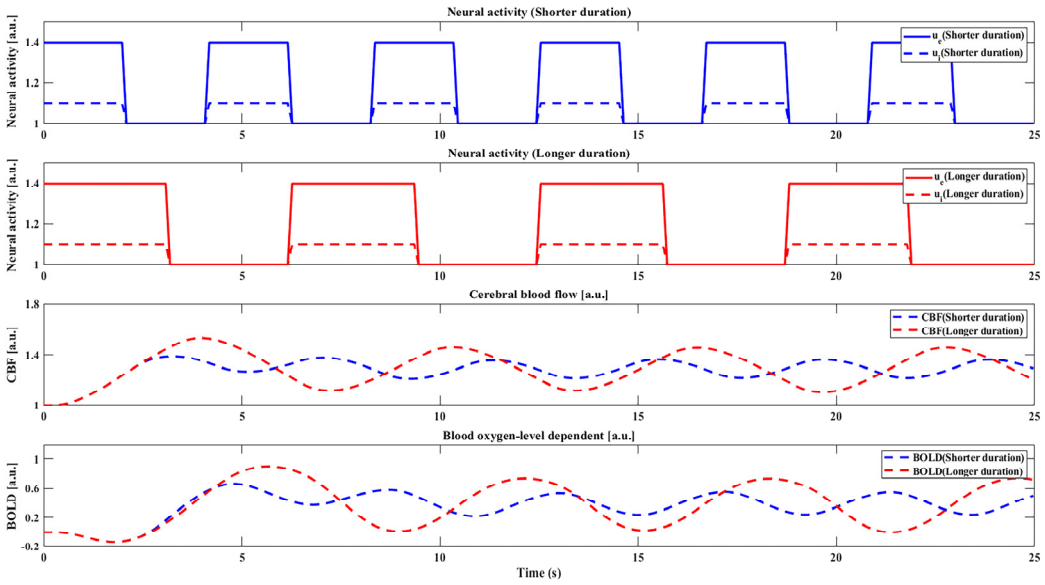

Figure 2. Hemodynamic metrics induced by neural activities of different durations. From top to bottom, the metrics are neural activity, CBF, and BOLD. The neural stimuli with shorter and longer durations are 1.98 s and 3.08 s, respectively (shorter duration in blue, longer duration in red).

Reference

1. N. Tzourio-Mazoyer, B. Landeau, D. Papathanassiou, F. Crivello, O. Etard, N. Delcroix, et al., Automated anatomical labeling of activations in SPM using a macroscopic anatomical parcellation of the MNI MRI single-subject brain, *NeuroImage*, **15** (2002), 273–289. https://doi.org/10.1006/nimg.2001.0978

2. P. Hagmann, L. Cammoun, X. Gigandet, R. Meuli, C. J. Honey, V. J. Wedeen, et al., Mapping the structural core of human cerebral cortex, *PLoS Biol.*, **6** (2008), e159. https://doi.org/10.1371/journal.pbio.0060159
3. R. S. Desikan, F. Ségonne, B. Fischl, B. T. Quinn, B. C. Dickerson, D. Blacker, et al., An automated labeling system for subdividing the human cerebral cortex on MRI scans into gyral based regions of interest, *NeuroImage*, **31** (2006), 968–980. https://doi.org/10.1016/j.neuroimage.2006.01.021
4. K. Brodmann, *Vergleichende Lokalisationslehre der Grosshirnrinde, in ihren Prinzipien dargestellt auf Grund des Zellenbaues*, Leipzig, 1909.
5. S. Demont-Guignard, P. Benquet, G. Coiret, U. Gerber, F. Wendling, Interpretation of intracerebral-EEG epileptic spikes from detailed modeling of neural networks, in *2009 4th International IEEE/EMBS Conference on Neural Engineering*, (2009), 530–533. https://doi.org/10.1109/NER.2009.5109350
6. B. H. Jansen, V. G. Rit, Electroencephalogram and visual evoked potential generation in a mathematical model of coupled cortical columns, *Biol. Cybern.*, **73** (1995), 357–366. https://doi.org/10.1007/BF00199471
7. R. C. Sotero, N. J. Trujillo-Barreto, Modelling the role of excitatory and inhibitory neuronal activity in the generation of the BOLD signal, *NeuroImage*, **35** (2007), 149–165. https://doi.org/10.1016/j.neuroimage.2006.10.027
8. K. J. Friston, A. Mechelli, R. Turner,C. J. Price, Nonlinear responses in fMRI: The Balloon model, Volterra kernels, and other hemodynamics, *NeuroImage*, **12** (2000), 466–477. https://doi.org/10.1006/nimg.2000.0630
9. R. B. Buxton, K. Uludağ, D. J. Dubowitz, T. T. Liu, Modeling the hemodynamic response to brain activation, *NeuroImage*, **23** (2004), S220–S233. https://doi.org/10.1016/j.neuroimage.2004.07.013
10. M. Rubinov, O. Sporns, Complex network measures of brain connectivity: Uses and interpretations, *NeuroImage*, **52** (2010), 1059–1069. https://doi.org/10.1016/j.neuroimage.2009.10.003
11. M. Barthelemy, Betweenness centrality in large complex networks, *Eur. Phys. J. B*, **38** (2004), 163–168. https://doi.org/10.1140/epjb/e2004-00111-4

AIMS Press